

RSC Advances



This is an *Accepted Manuscript*, which has been through the Royal Society of Chemistry peer review process and has been accepted for publication.

Accepted Manuscripts are published online shortly after acceptance, before technical editing, formatting and proof reading. Using this free service, authors can make their results available to the community, in citable form, before we publish the edited article. This *Accepted Manuscript* will be replaced by the edited, formatted and paginated article as soon as this is available.

You can find more information about *Accepted Manuscripts* in the [Information for Authors](#).

Please note that technical editing may introduce minor changes to the text and/or graphics, which may alter content. The journal's standard [Terms & Conditions](#) and the [Ethical guidelines](#) still apply. In no event shall the Royal Society of Chemistry be held responsible for any errors or omissions in this *Accepted Manuscript* or any consequences arising from the use of any information it contains.

Oxygen-octahedral distortion and electronic correlation induced semiconductor gaps in ferrimagnetic double perovskite Ca_2MReO_6 ($M=\text{Cr,Fe}$)

Sai Gong, San-Dong Guo, Peng Chen and Bang-Gui Liu*

*Beijing National Laboratory for Condensed Matter Physics,
Institute of Physics, Chinese Academy of Sciences, Beijing 100190, China*

(Dated: July 11, 2015)

Motivated by experimental nonmetallic features and high magnetic Curie temperatures of 360 and 522 K in double perovskite $\text{Ca}_2\text{CrReO}_6$ and $\text{Ca}_2\text{FeReO}_6$, we systematically investigate the structural, electronic, and magnetic properties of Ca_2MReO_6 ($M=\text{Cr,Fe}$) by combining the modified Becke-Johnson (mBJ) exchange potential with usual generalized gradient approximation (GGA). Our full optimization leads to stable ground-state structures with monoclinic symmetry ($P2_1/n$) consistent with experiment. The mBJ calculation successfully produces ferrimagnetic phase with semiconductor gaps of 0.38 eV and 0.05 eV, respectively, in contrast with wrong metallic phases from GGA calculations. With the spin-orbit coupling (SOC) taken into account, the Ca_2MReO_6 ($M=\text{Cr,Fe}$) shows high magneto-crystalline anisotropy (MCA) with the magnetic easy axis along the [010] direction. Although reducing to 0.31 and 0.03 eV, the semiconductor gaps remain open in spite of the SOC broadening of the Re t_{2g} bands. Therefore, our DFT investigation has established the correct ferrimagnetic semiconductor ground states for the double perovskite Ca_2MReO_6 ($M=\text{Cr,Fe}$) materials. Our analysis shows that the semiconductor gaps are due to orbital-selective splitting on Re t_{2g} bands in the minority-spin channel, originated from the O-octahedral distortion and Coulomb correlation effect. This mechanism, different from that in other double perovskite materials such as $\text{Sr}_2\text{CrOsO}_6$, $\text{Ca}_2\text{CrOsO}_6$ and $\text{Sr}_2\text{FeOsO}_6$, can be useful to fully understand chemical and physical properties of double perovskite compounds.

PACS numbers: 75.30.-m, 75.50.-y, 75.10.-b, 71.20.-b

I. INTRODUCTION

Because of their rich physics and high technological potential¹, ordered double perovskite $A_2BB'O_6$ (A = alkali, alkaline-earth or rare-earth ion; B and B' = transition metals) have been extensively studied²⁻¹⁸. For cubic or tetragonal double perovskite $\text{Sr}_2BB'O_6$ (B = Cr or Fe, and B' = Mo, W, or Re), ferrimagnetic metallic phase is usually formed because the fully occupied high spin state Fe^{3+} ($3d^5$) or Cr^{3+} ($3d^3$) is antiferromagnetically coupled with the partially filled $4d$ and $5d$ transition-metal cations^{18,19}. Among them, half-metallic $\text{Sr}_2\text{FeMoO}_6$, $\text{Sr}_2\text{FeReO}_6$, and $\text{Sr}_2\text{CrReO}_6$ have been known as prospective spintronic materials beyond room temperature^{3,5,10,18,20}. On the other hand, double perovskite $\text{Sr}_2\text{CrOsO}_6$ is a robust ferrimagnetic insulator with the highest magnetic Curie of 725 K, and its semiconductor gap has been shown to originate from spin-exchange splitting of the Os $5d$ t_{2g} bands^{18,21,22}. With the same origin of band gap, the recently crystallized $\text{Ca}_2\text{FeOsO}_6$ presents an insulating ferrimagnetic phase below 320 K^{23,24}. Another compound $\text{Sr}_2\text{FeOsO}_6$ is also revealed to be an insulator in spite of antiferromagnetic arrangement^{25,26}. Very special are double perovskite $\text{Ca}_2\text{FeReO}_6$ and $\text{Ca}_2\text{CrReO}_6$. It is shown experimentally that they are ferrimagnetic insulators with monoclinic structure and have high magnetic Curie temperatures of 522 and 360 K^{9,14,18,20,27,39}, but their non-metallic electronic properties have not yet been elucidated although some efforts were made for the $\text{Ca}_2\text{FeReO}_6$ material^{40,41}. In addition, their structure-property relationship needs

to be understood.

Here, we investigate the structural, electronic and magnetic properties of the $\text{Ca}_2\text{CrReO}_6$ and $\text{Ca}_2\text{FeReO}_6$ through density functional theory calculations in order to reveal the origin of their special electronic structures, especially their semiconductor gaps at low temperature. We use Tran and Blahos modified Becke and Johnson (mBJ) approach for the exchange potential²⁸ to investigate their electronic structures because its excellent accuracy has been proved for most of insulators, semiconductors, and transition-metal oxides²⁸⁻³¹. Our calculations reveal that the $\text{Ca}_2\text{CrReO}_6$ and $\text{Ca}_2\text{FeReO}_6$ are both ferrimagnetic semiconductors, even with the spin-orbit effect taken into account. Our further analysis shows that the semiconductor gaps are formed between the full-filled d_{xz} and the empty d_{yz} states around the Fermi level due to the mutual cooperation of O-octahedral distortion and Coulomb correlation. We also explore other properties of the two Ca-based double perovskite compounds in comparison with similar materials. More detailed results will be presented in the following.

The rest of the paper is organized as follows. We shall describe our computational details in the next section. In Sec. III we shall present our optimized ground-state structures for the two compounds. In Sec. IV we shall present our spin-dependent density of states, band structures, and electron density distributions and perform further analyses concerned. In Sec. V we shall present our calculated results with the spin-orbit effect taken into account, including their magneto-crystalline anisotropic energies, spin and orbital moments along the easy axis, and the spin-orbit-effect-modified semiconductor gap.

Finally, we shall give our conclusion in Sec. VI.

II. COMPUTATIONAL DETAILS

We use the full-potential linear augmented plane wave (FP-LAPW) method within the density functional theory (DFT),^{32,33} as implemented in the WIEN2k package.³⁴ We take GGA exchange-correlation functional to do structure optimization and preliminary study³⁵, and then use mBJ exchange potential to do electronic structure calculations. The scalar relativistic approximation is used for valence states, with the spin-orbit coupling (SOC) is taken into account, whereas the radial Dirac equation is self-consistently solved for the core electrons³⁶⁻³⁸. The magnetization is chosen to be along all nonequivalent directions for the monoclinic structure when we investigate the magneto-crystalline anisotropy. The muffin-tin radii of the Ca, Cr, Fe, Re, and O atoms are set to be 2.20, 1.96, 2.03, 1.96, and 1.71 bohr, respectively. We make harmonic expansion up to $l_{max} = 10$ in the muffin-tin spheres, and set $R_{mt} \times K_{max} = 8.0$. We use 1000 k-points in whole Brillouin zone (234 k-points in the reduced wedge). For testing the accuracy, we also use 2000 k-points in whole Brillouin zone (576 k-points in the reduced wedge) to do the self-consistent calculations. The total energy difference is proved to be less than 1 meV. Therefore, our choice of 1000 k-points is enough for the whole calculation. The self-consistent calculations are considered to be converged only when the integration of absolute charge-density difference per formula unit between the successive loops is less than $0.0001|e|$, where e is the electron charge.

III. STRUCTURE OPTIMIZATION

The structure of Ca_2MReO_6 ($M=\text{Cr}$ or Fe) has been reported to be monoclinic structure with $P2_1/n$ symmetry (space group #14) at room temperature,^{9,18} which is consistent with the prediction of the empirical tolerance factor f .^{18,39} The monoclinic structure is fairly distorted from cubic double perovskite due to the small size of Ca^{2+} cation, which forces the MO_6 and ReO_6 octahedra to tilt and rotate in order to optimize the Ca-O bond lengths. As a representative, we demonstrate the the crystal structure of $\text{Ca}_2\text{CrReO}_6$ in Fig. 1. Both $P2_1/n$ and $I4/m$ structures are presented for the following discussion. In order to investigate the origin of the nonmetallicity in their ground-state phases, we optimize fully their geometric structures and internal atomic positions by combining total energy and force optimizations. We have considered a larger unit cell of 2 f.u. including 20 atoms to relax the structure. The optimized lattice parameters are listed in Table I, with experimental data included for comparison. Our total energy calculations show that the ground state phase is the $P2_1/n$ structure for both of the compounds, with lattice constants ex-

panded slightly with respect to experimental ones. This deviation is due to the special property of the GGA functional. However, the tilt angles β of Ca_2MReO_6 ($M=\text{Cr}$ and Fe) decrease by 0.22° and 0.27° with respect to experimental values, respectively, which reflects the large distortion at low temperature.

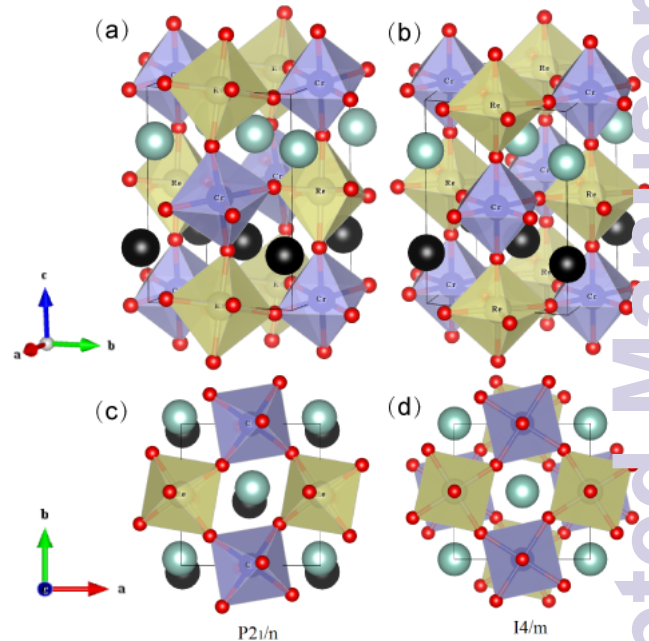


FIG. 1: (color online) (a) Crystal structure of double perovskite $\text{Ca}_2\text{CrReO}_6$ with 2 unit cells in $P2_1/n$ (#14) symmetry, (b) the $I4/m$ (#87) structure is displayed for comparison, (c) and (d) the projected images in the (110) plane for corresponding structures. CrO_6 and ReO_6 octahedra are denoted with purple and yellow, respectively. The green and black ones are Ca atoms in two different layers.

TABLE I: Optimized lattice constants and tilt angle β of Ca_2MReO_6 ($M=\text{Cr,Fe}$) with space group $P2_1/n$ (#14), compared with experimental results⁹

Lattice parameters	$\text{Ca}_2\text{CrReO}_6$		$\text{Ca}_2\text{FeReO}_6$	
	opt.	exp.	opt.	exp.
a (\AA)	5.392	5.388	5.417	5.401
b (\AA)	5.524	5.460	5.609	5.525
c (\AA)	7.680	7.660	7.733	7.664
β ($^\circ$)	89.74	89.96	89.80	90.07

We present in Table II optimized bond lengths and bond angles of Ca_2MReO_6 ($M=\text{Cr,Fe}$) with $P2_1/n$ structure. For comparison, we also present the $I4/m$ structure for $\text{Ca}_2\text{CrReO}_6$. It's shown that the three Ca-O bond lengths are slightly larger than Re-O ones in $\text{Ca}_2\text{CrReO}_6$, while the FeO_6 octahedra are significantly more expanded than ReO_6 octahedra in $\text{Ca}_2\text{FeReO}_6$. This observation is consistent with the ionic size sequence of $\text{Re}^{5+} < \text{Cr}^{3+} < \text{Fe}^{3+}$. The bond angles in ReO_6 octa-

hedra all deviate from ideal values of 90° , so do the angles of M -O-Re from 180° . Considering that a large number of double perovskite compounds with half-metallicity are in tetragonal structure with $I4/m$ symmetry (space group #87), and in order to clarify the relationship between the electronic property and lattice structure, we also present the structure parameters of the $I4/m$ structure for $\text{Ca}_2\text{CrReO}_6$ in Table II. There are actually two nonequivalent kinds of O atoms in $I4/m$ structure. The O_1 and O_2 atoms are equal to each other and in the same xy -plane. The atom O_3 sits along the z -axis with Cr or Re atoms in between. The bond lengths of Cr-O are larger than those of Re-O due to the larger ionic size of Cr^{3+} versus Re^{5+} . All angles in ReO_6 octahedra remain to be 90° , while the Cr- $\text{O}_{1,2}$ -Re bond angles reduce significantly from 180° , which makes the Cr- $\text{O}_{1,2}$ and Re- $\text{O}_{1,2}$ lengths much larger than the Cr- O_3 and Re- O_3 bonds, respectively. Our calculated total energy of $\text{Ca}_2\text{CrReO}_6$ in $I4/m$ structure are higher than that in $P2_1/n$ structure by 392 meV per formula unit, indicating the $P2_1/n$ structure is more stable for $\text{Ca}_2\text{CrReO}_6$.

TABLE II: Optimized bond lengths and angles of Ca_2MReO_6 ($M=\text{Cr}, \text{Fe}$) with space group $P2_1/n$ (#14), with those of $\text{Ca}_2\text{CrReO}_6$ with $I4/m$ (#87) structure for comparison. O_1 and O_2 are equivalent to each other in $I4/m$ structure.

	M	Cr(#14)	Cr(#87)	Fe(#14)
Bond length	M- O_1	1.975	1.984	2.061
	M- O_2	1.978	1.984	2.046
	M- O_3	1.971	1.939	2.036
	Re- O_1	1.974	1.977	1.944
	Re- O_2	1.968	1.977	1.948
	Re- O_3	1.964	1.922	1.941
	Bond angle	O_1 -Re- O_2	90.88	90
O_2 -Re- O_3		89.43	90	89.28
O_1 -Re- O_3		89.81	90	89.22
M- O_1 -Re		152.56	154.63	149.34
M- O_2 -Re		152.85	154.63	150.59
M- O_3 -Re		153.46	180	150.06

IV. ELECTRONIC STRUCTURES

A. Density of states and energy bands

From now on, we investigate the electronic structures of the optimized Ca_2MReO_6 ($M=\text{Cr}, \text{Fe}$). At first, we use the popular GGA functional to calculate the density of states (DOS). The spin-resolved DOSs are presented in Fig. 2. For the $\text{Ca}_2\text{CrReO}_6$, the electronic energy bands between -8.0 eV and -3.0 eV are dominated by O $2p$ states. The Fermi energy falls in an energy gap of about 1.0 eV in the majority spin channel, between the fully filled Cr t_{2g} and empty Re t_{2g} bands. As for

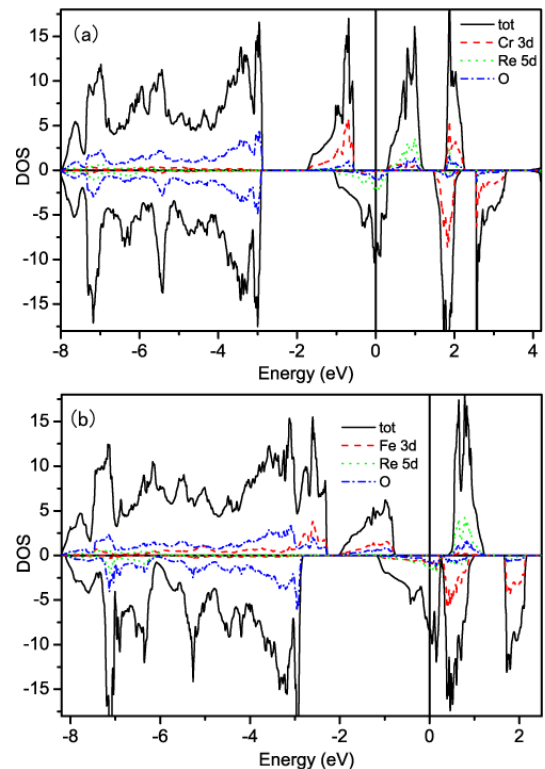


FIG. 2: (color online) The spin-resolved total (tot) and partial (Cr/Fe,Re,O) density of states (DOSs) of $\text{Ca}_2\text{CrReO}_6$ (a) and $\text{Ca}_2\text{FeReO}_6$ (b) in $P2_1/n$ structure from GGA calculation.

the $\text{Ca}_2\text{FeReO}_6$, the triplet Fe t_{2g} states in the majority spin channel move to the lower energy between -8.2 eV and -2.2 eV, with a strong mixture of O $2p$ states. The Fermi energy is in the majority-spin gap of 1.4 eV between Fe e_g and Re t_{2g} bands. In contrast, for the minority spin channel, the Fermi level lies in the partially filled t_{2g} bands of hybridized M , Re, and O $2p$ states in the Ca_2MReO_6 ($M=\text{Cr}, \text{Fe}$). Thus, the GGA calculation produces a half-metallic ferrimagnet. This is contradictory with the reported experimental results^{9,18} and can be attributed to the false GGA description of Re t_{2g} nature around the Fermi level in the monoclinic structure. For the sake of accurate calculation for Re t_{2g} state, we need to use improved exchange potential to investigate the electronic structures of the Ca_2MReO_6 . The modified Becke-Johnson (mBJ) potential is a good choice because it is excellent in describing the hybrid transition-metal ions.^{29,42}

We present the spin-resolved DOSs and energy bands of the $\text{Ca}_2\text{CrReO}_6$ calculated with mBJ in Fig. 3. It is clear that there is a semiconductor gap open at the Fermi level, which is in good agreement with experimental results⁹. Moreover, the occupied Cr t_{2g} and unoccupied Cr e_g and Re t_{2g} bands in the majority spin channel are pushed substantially downwards and upwards, respectively, which consequently enhances the majority-spin gap (G_{mag}) to 2.5 eV. In the minority spin channel,

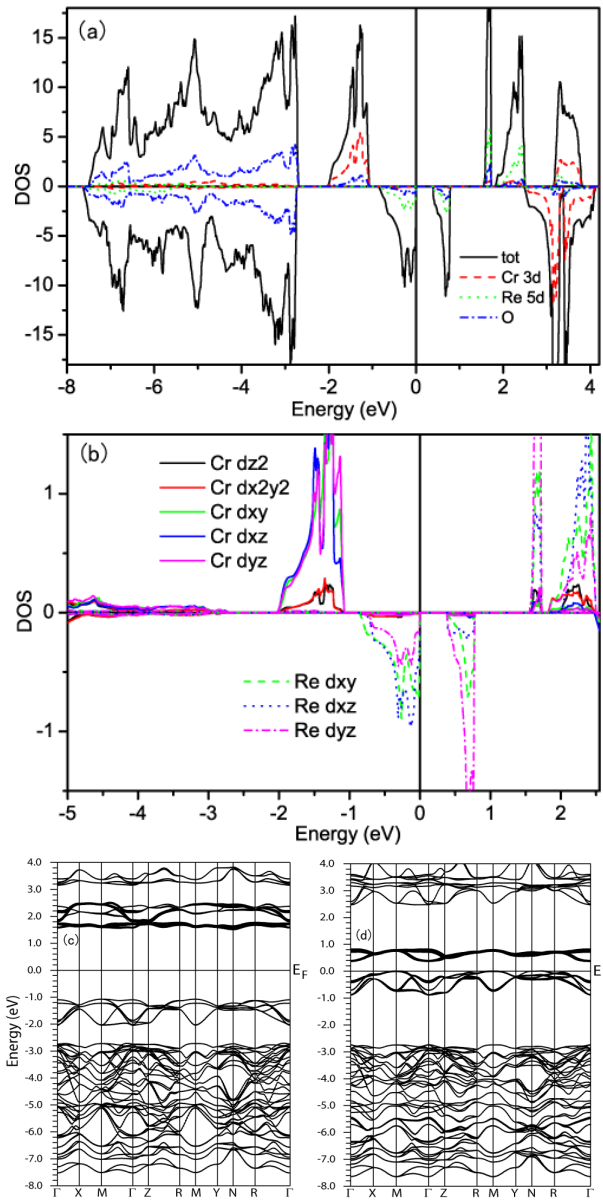


FIG. 3: (color online) Electronic structure of $\text{Ca}_2\text{CrReO}_6$ in $P2_1/n$ structure calculated with mBJ: spin-resolved total (tot) and partial (Cr,Re,O) DOSs (a); amplified d states split DOSs of Cr and Re around the Fermi level (b); and majority-spin (c) and minority-spin (d) bands.

the triplet Re t_{2g} states around the Fermi level split into a doublet $d_{xy}+d_{xz}$ and a singlet d_{yz} , with two electrons fully occupying the doublet state. This produces a semiconductor gap of 0.38 eV, as shown in Fig. 3(a). The detailed orbital-resolved DOSs around the Fermi level are presented in Fig. 3(b). Both of the unoccupied Cr t_{2g} and e_g in the minority spin channel are pushed upwards substantially, with a little overlap between them, which enlarges the spin exchange splitting energy of Cr t_{2g} to 4.7 eV. Fig. 3(c) and (d) show the energy bands of the $\text{Ca}_2\text{CrReO}_6$ in majority-spin and minority-spin channels,

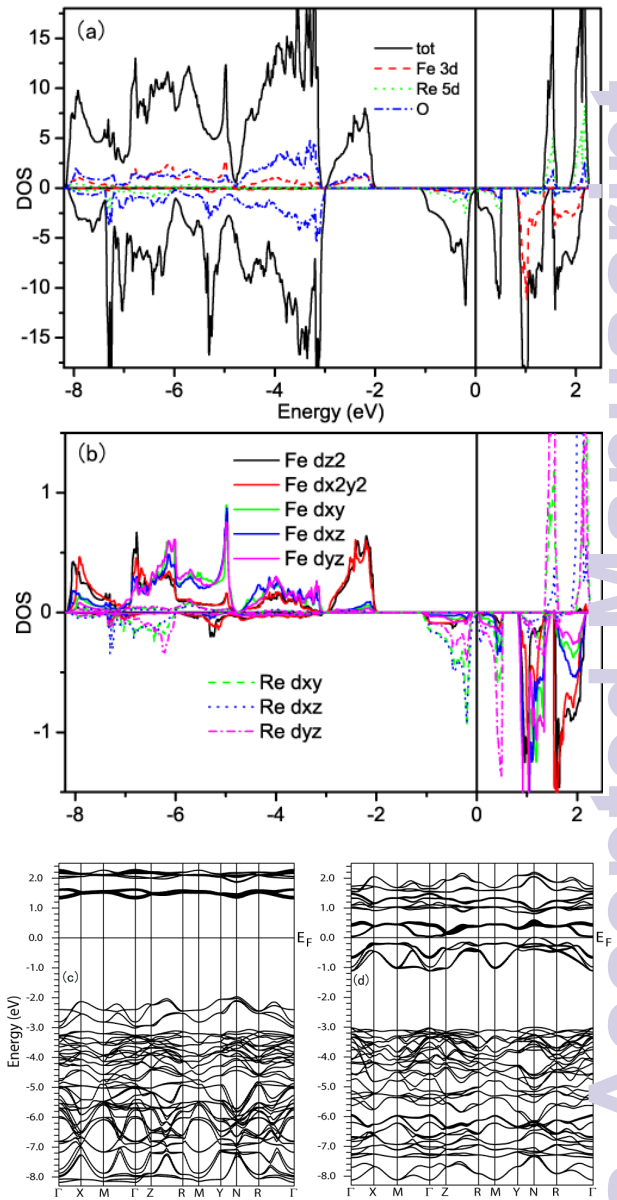


FIG. 4: (color online) Electronic structure of $\text{Ca}_2\text{FeReO}_6$ in $P2_1/n$ structure calculated with mBJ: spin-resolved total (tot) and partial (Fe,Re,O) DOSs (a); amplified d states split DOSs of Fe and Re around the Fermi level (b); and majority-spin (c) and minority-spin (d) bands.

respectively. The thicker a line is, the more the Re t_{2g} weight is. There are 72 bands (36 majority spin and 36 minority spin) in the energy window from -7.8 eV to -2.0 eV, because we consider 2 unit cell in our calculation. The energy bands between -2.0 eV and -1.0 eV consist of 6 Cr t_{2g} bands in the majority spin channel. There are 4 occupied bands of Re t_{2g} , including d_{xy} and d_{xz} just below the Fermi level and 2 bands of d_{yz} above the Fermi level. It can be clearly seen that the top of the valence band and the bottom of the conduction band are located in M and Γ points, respectively, resulting in an indirect band gap for the $\text{Ca}_2\text{CrReO}_6$.

In Fig. 4 we present the spin-resolved DOSs and energy bands of the optimized $\text{Ca}_2\text{FeReO}_6$ calculated with mBJ. The distinguished feature of the DOSs is that compared to GGA results, the Fe t_{2g} states move to lower energy in the majority spin channel, and the gaps between Fe t_{2g} and e_g states almost vanish in both of spin channels. This can be attributed to the enhanced spin exchange effect due to mBJ functional. The semiconductor gap of 0.05eV is also observed, owing to the same reason as in the $\text{Ca}_2\text{CrReO}_6$. However, the Re t_{2g} splitting in the minority spin channel is much smaller than that in the majority spin channel, in contrast to the $\text{Ca}_2\text{CrReO}_6$. This result is consistent with the fact that the resistivity of the $\text{Ca}_2\text{FeReO}_6$ at low temperature is almost two order of magnitude lower than that of $\text{Ca}_2\text{CrReO}_6$, because the electron inter-band transition takes place easily in the $\text{Ca}_2\text{FeReO}_6$ compound. In the band structures (c) and (d) of the $\text{Ca}_2\text{FeReO}_6$, the Fe t_{2g} bands are pushed down to between -8.0 eV and -3.0 eV in the majority spin channel, in contrast to the minority-spin one. The energy window from -3.0 eV to -2.0 eV consists of 4 bands of Fe e_g . The top of valence bands and the bottom of the conduction bands are located in N and Γ points, respectively. This implies that the semiconductor gap of the $\text{Ca}_2\text{FeReO}_6$ is indirect, same as that of the $\text{Ca}_2\text{CrReO}_6$.

B. Electron density distributions

The energy-resolved charge and spin density distributions are very important to explore the bonding and magnetic properties. We present in Fig. 5 the valence charge (including up and down) and spin density distributions of the $\text{Ca}_2\text{CrReO}_6$, with all the contribution from -8.0 eV to the Fermi level, calculated with mBJ. The upper three panels are for the (001) plane of the structure shown in Fig. 1, the lower three ones are for the perpendicular plane, being equivalent to the (110) plane, including Cr and Re ions. In the spin-up channel, the charge density distributions at Cr sites look like a quatrefoil, which reflects the fully occupied t_{2g} characteristic between -2 eV to -1 eV, whereas the charge density around Re is fairly small. In the spin-down channel, there is much electron density around Re, in consistence with the partially filled Re t_{2g} state from -1 eV to the Fermi level. The small charge density at Cr sits should result from the hybridization between Re and Cr t_{2g} states. In both of the spin channels, the oxygen atoms with high electron affinities attract the electrons from Cr and Re atoms to form nearly closed O $2p$ shells with spherically distributed charge densities. It can be seen in the charge density contours that the bonds between Cr and nearest O are almost ionic with respect to the Re-O bonds with covalent characteristic, which is in accordance with the longer bond lengths of Cr-O than Re-O ones, as described in Table II. The charge distributions also show that there exists no direct interaction between two nearest Cr-Cr or Re-Re pairs. The spin density distribution of the $\text{Ca}_2\text{CrReO}_6$ in Fig.

5 (e) and (f) demonstrates that the spin moments of Cr and Re are mainly localized at the ionic sites. The contours, with an increment of $0.013\mu_B/\text{a.u.}^3$, mean that the spin density around Cr varies from $-0.5\mu_B/\text{a.u.}^3$ to 0 and that around Re from 0 to $0.5\mu_B/\text{a.u.}^3$. This spin density distribution indicates the antiferromagnetic coupling between the Cr and Re moments in the double perovskite $\text{Ca}_2\text{CrReO}_6$. The some deformed quatrefoils of Cr and Re ions are ascribed to the distortion of O octahedra. It is worth note that different density contours between Re and Cr sites are due to the more closed shells in the inner part of heavier Re ion compared to Cr.

As for the $\text{Ca}_2\text{FeReO}_6$, we illustrate the corresponding charge and spin density distributions calculated with mBJ in Fig. 6. It can be seen that charge distributions at the Fe site are nearly spherical because of nearly half-filled Fe $3d$ orbitals, which is different from the quatrefoils shape of partially occupied Cr $3d$ orbitals in the $\text{Ca}_2\text{CrReO}_6$. The Fe $3d$ electrons that are more than half full move to oxygen sites for stabilizing the ground state, leaving the highly ionized Fe atoms, as shown in Fig. 6. The shape of charge density around the Re site is similar to that in the $\text{Ca}_2\text{CrReO}_6$ due to the same valence states of Re^{5+} ions in the two compounds. Most of the Re $5d$ electrons with larger orbitals spread out to O $2p$ states, forming the Re-O covalent bonds. Furthermore, the hybridizations are still along the Fe-O-Re-O-Fe chain and no direct interaction between Fe-Fe and Re-Re pairs are found. The spin moments of Fe $3d$ and Re $5d$ states are mainly localized and coupled antiferromagnetically, as are those of the Cr and Re states in the $\text{Ca}_2\text{CrReO}_6$.

TABLE III: Spin exchange splitting (Δ_{ex}) and crystal field splitting (Δ_{cf}) of Cr and Fe, spin exchange splitting Δ_{ex} of Re ion, the band gaps across the Fermi level in the majority spin channel (G_{maj}) and the minority-spin channel (G_{min}) of Ca_2MReO_6 ($M=\text{Cr, Fe}$) calculated with GGA and mBJ.

M	scheme	$\Delta_{\text{ex}}(M)$	$\Delta_{\text{cf}}(M)$	$\Delta_{\text{ex}}(\text{Re})$	G_{maj}	G_{min}
Cr	GGA (eV)	2.9	3.0	0.8	1.0	0
	mBJ (eV)	4.6	6.7	2.0	2.5	0.5
Fe	GGA (eV)	3.0	1.0	0.7	1.4	0
	mBJ (eV)	6.5	3.0	1.8	3.3	0.05

C. Further analyses

The spin exchange splitting (Δ_{ex}) and crystal field splitting (Δ_{cf}) of Cr and Fe, the spin exchange splitting Δ_{ex} of Re ion, and the band gaps across the Fermi level in both majority-spin (G_{maj}) and minority-spin (G_{min}) channels calculated with GGA and mBJ are summarized in Table III. Here, the spin exchange splitting energy of Cr (Fe) is defined as the energy difference between the DOS weight centre of the filled Cr- t_{2g} (Fe- $3d$) spin-up states and that of the empty Cr- t_{2g} (Fe- $3d$) spin-down states.

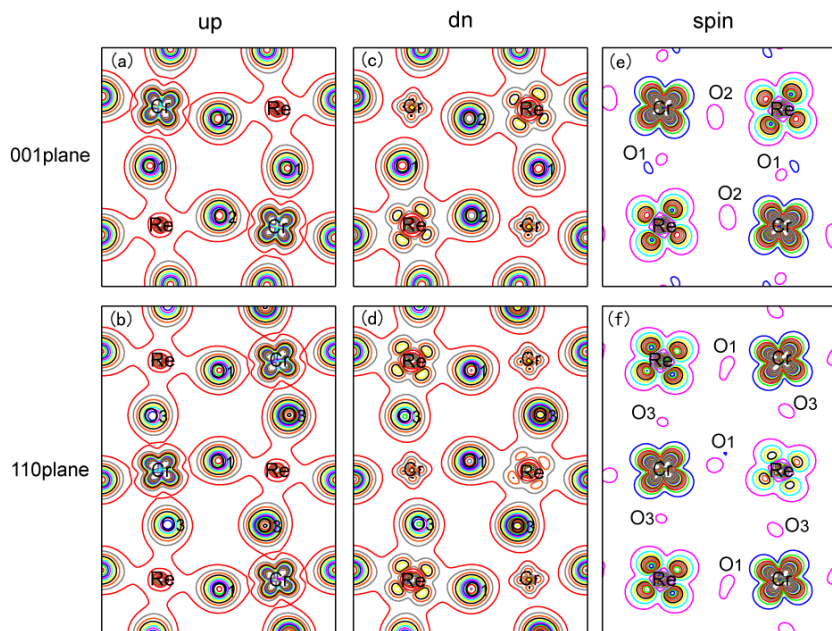


FIG. 5: (color online) Valence electron charge [up, (a) and (b); dn, (c) and (d)] and spin [(e),(f)] density distributions, within the energy window from -8.0 eV to the Fermi level, of $\text{Ca}_2\text{CrReO}_6$ projected to the (001) and (110) planes calculated with mBJ. The contours in (a)-(d) are from 0.005 to $0.5e/\text{a.u.}^3$ with an increment of $0.025e/\text{a.u.}^3$, and those in (e) and (f) from -0.5 to $0 \mu_B/\text{a.u.}^3$ for Re sites and 0 to $0.5\mu_B/\text{a.u.}^3$ for Cr sites with an increment of $0.013\mu_B/\text{a.u.}^3$.

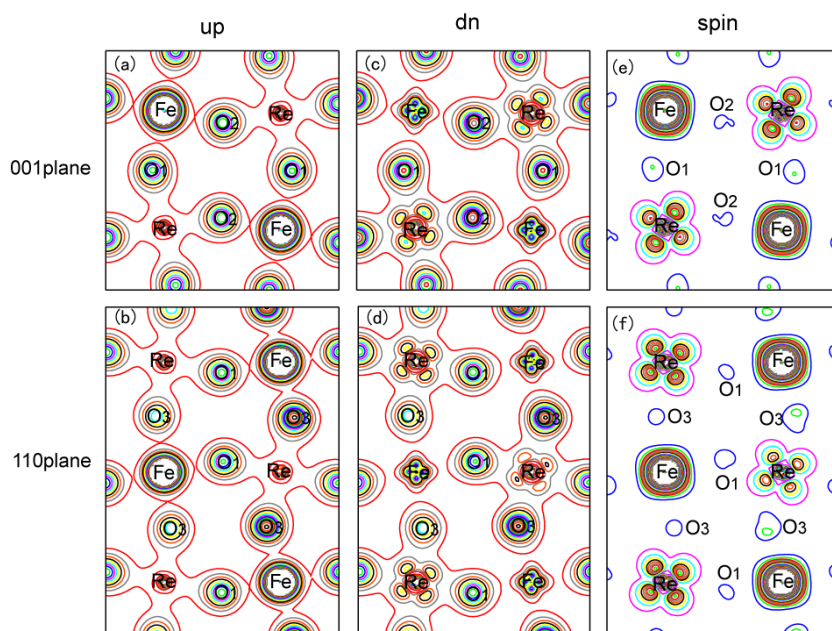


FIG. 6: (color online) Valence electron charge [up, (a) and (b); dn, (c) and (d)] and spin [(e),(f)] density distributions, within the energy window from -8.2 eV to the Fermi level, of $\text{Ca}_2\text{FeReO}_6$ projected to the (001) and (110) planes calculated with mBJ. The contours in (a)-(d) are from 0.005 to $0.5e/\text{a.u.}^3$ with an increment of $0.025e/\text{a.u.}^3$, and those in (e) and (f) from -0.5 to $0 \mu_B/\text{a.u.}^3$ for Re sites and 0 to $0.5\mu_B/\text{a.u.}^3$ for Fe sites with an increment of $0.013\mu_B/\text{a.u.}^3$.

ones, and for Re it is similarly defined as the energy difference between the partially filled spin-down $5d$ states and those empty spin-up ones. Both Δ_{ex} and Δ_{cf} of transition-metals are significantly enhanced by mBJ calculation. As a result, the gaps in the majority spin channel are enlarged by 1.5 eV and 1.9 eV for the Ca_2MReO_6 ($M=\text{Cr},\text{Fe}$), respectively. The semiconductor gaps are equivalent to 0.38 eV and 0.05 eV, respectively, in contrast to the wrong results from GGA. This implies that electron correlations play an essential role in forming semiconductivity on Ca_2MReO_6 ($M=\text{Cr},\text{Fe}$) compounds due to the mBJ approach mimics the behavior of orbital-dependent potentials and the correlation effects are treated not only for localized, but also for delocalized electron-

s. The role of correlations can also be verified by the fact that the Ca_2CrWO_6 shows insulator behavior⁴³, while $\text{Ca}_2\text{FeMoO}_6$ exhibits metallic conduction⁴⁴, which is attributed to the stronger correlation strength in $5d$ atoms of W and Re than $4d$ one of Mo.

Besides electron correlations, we also investigate the effect of lattice structure on opening band gaps of Ca_2MReO_6 ($M=\text{Cr},\text{Fe}$). The DOSs of the $\text{Ca}_2\text{CrReO}_6$ in $I4/m$ structure with both GGA and mBJ functionals are presented in Fig. 7. It's shown that the GGA produces a half-metallicity, which is similar to the GGA result of the $\text{Ca}_2\text{CrReO}_6$ with $P2_1/n$ symmetry, and however, the metallic property is not changed by using mBJ potential, although the Δ_{ex} and Δ_{cf} of Cr

and Re are much enlarged. This comparison indicates that the semiconductor nature of the Ca_2MReO_6 has intimate relationship with the crystal structure. For discussing the importance of structure in detail, We present in Fig. 8 the band structures near the Fermi level in the minority-spin channel, showing the Re 5d states for the $\text{Ca}_2\text{CrReO}_6$. The corresponding states of the $\text{Ca}_2\text{FeReO}_6$ are similar to those of the $\text{Ca}_2\text{CrReO}_6$. In the $I4/m$ structure, the bond angles of CrO_6 and ReO_6 octahedra are ideal 90° , as shown in Fig. 1 (b), allowing the symmetry operation of rotation 45° and translation along z axis. Therefore, the Re 5d states are preserved in high degeneracy. The d_{xy} bands are full-occupied with two electrons and lie below the Fermi level. The remainder two ones half-fill the doublet $d_{xz}+d_{yz}$ states, resulting in the metallicity of the $\text{Ca}_2\text{CrReO}_6$. As for the $P2_1/n$ structure, the CrO_6 and ReO_6 octahedra undergo tilting and rotation, making the bond angles deviate from 90° . Meanwhile, the Ca atoms in different layers move oppositely, and then the symmetry along z axis is broken. The symmetry reduction urges the half-filled states to split into full-filled d_{xz} and empty d_{yz} ones, leading to a Peierls-like gap. This fact is consistent with the four-foil pattern of the spin density distribution at Re sites, as shown in Fig. 5(e) and (f) and Fig. 6 (e) and (f). In general, not only the correlation effect, but also octahedral distortion are necessary for the semiconductor nature of the Ca_2MReO_6 ($M=\text{Cr,Fe}$) compounds.

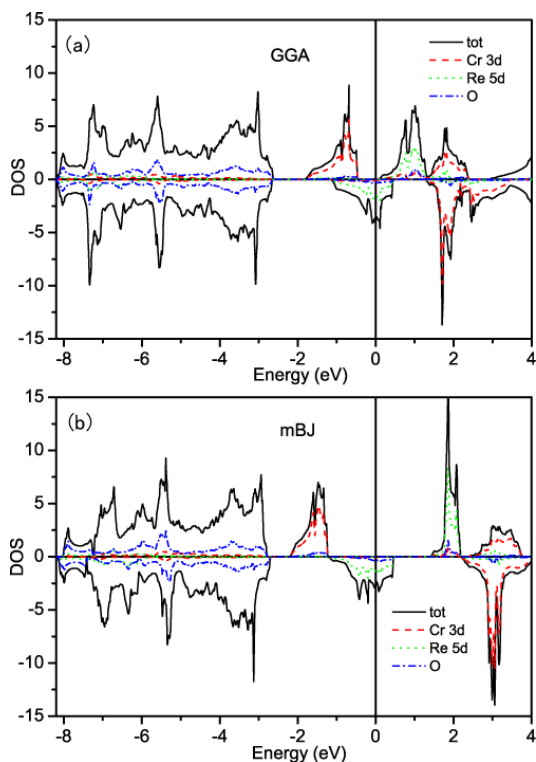


FIG. 7: (color online) The spin-resolved total and partial DOSs of $\text{Ca}_2\text{CrReO}_6$ in $I4/m$ structure with GGA (a) and mBJ (b) methods.

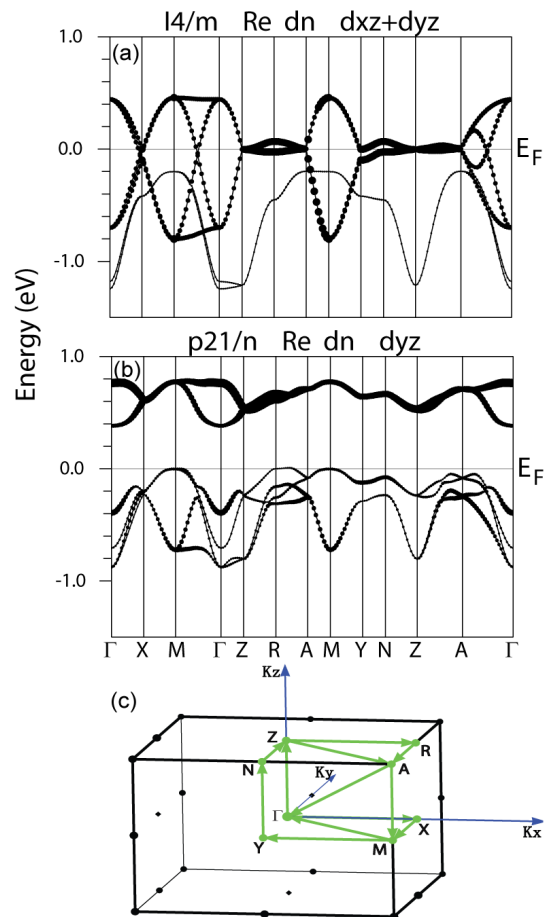


FIG. 8: (color online) The band structures near the Fermi level in the minority-spin channel of $\text{Ca}_2\text{CrReO}_6$ with $I4/m$ (a) and $P2_1/n$ (b) structures, respectively. The thick dot lines denote the $d_{xz}+d_{yz}$ of Re t_{2g} states for $I4/m$ and the d_{yz} state for $P2_1/n$ structure. The k -paths of both structures are displayed in (c).

V. SPIN-ORBIT COUPLING EFFECT

To investigate the effect of spin-orbit coupling on the optimized Ca_2MReO_6 ($M=\text{Cr,Fe}$), the magnetization is chosen to be approximately along $[100]$, $[010]$, $[001]$, $[110]$, $[101]$, $[011]$ and $[111]$ directions for the $P2_1/n$ monoclinic structure. The calculated total energies with GGA+SOC method presented in Table IV indicate high magnetocrystalline anisotropy (MAC) in the Ca_2MReO_6 compounds. The most stable magnetic orientation are both along $[010]$ direction, equivalent to the b -axis perpendicular to the ac plane in the $P2_1/n$ structure. These are consistent with experimental results¹⁸.

After the magnetic easy axis is fixed, we do further study with SOC along the $[010]$ direction. Our calculated spin and orbital moments for the Ca_2MReO_6 are summarized in Table V. When SOC is neglected, the total spin moment is precisely $1\mu_B$ and $3\mu_B$ per formula unit for the $\text{Ca}_2\text{CrReO}_6$ and $\text{Ca}_2\text{FeReO}_6$, respectively. If

TABLE IV: Total energies (meV) of Ca_2MReO_6 ($M=\text{Cr,Fe}$) with different magnetization orientations calculated with GGA+SOC, with the lowest energy set as reference.

M	[100]	[010]	[001]	[110]	[101]	[011]	[111]
Cr	1.00	0	2.16	1.21	2.08	1.34	1.29
Fe	1.37	0	2.04	2.03	2.62	1.60	1.61

TABLE V: The mBJ results of individual and total spin moments (μ^s), orbital moments (μ^o), and net moments (μ_{tot}) in μ_B , and semiconductor gap (G_s , in eV) of Ca_2MReO_6 ($M=\text{Cr,Fe}$) with $P2_1/n$ structure with and without SOC.

M	scheme	μ_M^s	μ_{Re}^s	μ_{tot}^s	μ_M^o	μ_{Re}^o	μ_{tot}	G_s
Cr	mBJ	2.520	-1.264	1.000			1.000	0.38
	mBJ+SOC	2.520	-1.239	1.035	-0.018	0.192	1.209	0.31
Fe	mBJ	4.090	-1.118	3.000			3.000	0.05
	mBJ+SOC	4.090	-1.096	3.033	0.042	0.183	3.258	0.03

results can be elucidated in the ionic model, where the transition-metal ions are in the $(M\text{Re})^{8+}$ valence state. The M^{3+} are in the high spin state of $S=3/2$ for Cr^{3+} and $S=5/2$ for Fe^{3+} according to Hund's rule, antiferromagnetically coupled with highly ionized Re^{5+} with valence spin states of $S=1$, resulting the integer moment in Bohr magneton. Note that a large part of the spin moment is delocalized into the interstitial region, and therefore the spin moments of the individual M and Re ions appear small compared to the ionic values.

When SOC is taken into account, the total spin moments increase by $0.035\mu_B$ and $0.033\mu_B$ for the Ca_2MReO_6 ($M=\text{Cr,Fe}$), respectively, due to some increase of Re spin moment. The orbital moments of Cr and Re are both antiparallel to the spin moments, because of the less than half-filled d shell, in accordance with Hund's rule. As for the $\text{Ca}_2\text{FeReO}_6$, the orbital moments of Fe $3d$ is of the same sign as the spin moment, indicating that the $3d$ orbital is more than half-filled, consistent with Hund's rule. Our calculated Cr orbital moment of $-0.018\mu_B$ is much smaller than the Fe one of $0.042\mu_B$, which could be understood as a consequence of stronger ligand field caused by the Cr $3d$ orbital than by the Fe $3d$ orbital. For Re ion, the orbital moment is $0.192\mu_B$ or $0.183\mu_B$ for the $\text{Ca}_2\text{CrReO}_6$ or $\text{Ca}_2\text{FeReO}_6$, due to the strong spin-orbit coupling in $5d$ orbital. The higher improvement of total magnetic moment, $0.258\mu_B$, in the $\text{Ca}_2\text{FeReO}_6$ than $0.209\mu_B$ in the $\text{Ca}_2\text{CrReO}_6$ is due to the positive large orbital moment in Fe ion.

We also present the semiconductor gaps G_s as the true gaps of these compounds in Table V. When SOC is included, the band gaps remain but become smaller, and is equivalent to 0.31 eV for the $\text{Ca}_2\text{CrReO}_6$ and 0.03 eV for the $\text{Ca}_2\text{FeReO}_6$, respectively. In order to understand in more detail the reason of the smaller gap with SOC, the partial DOS of M and Re projected onto d orbital

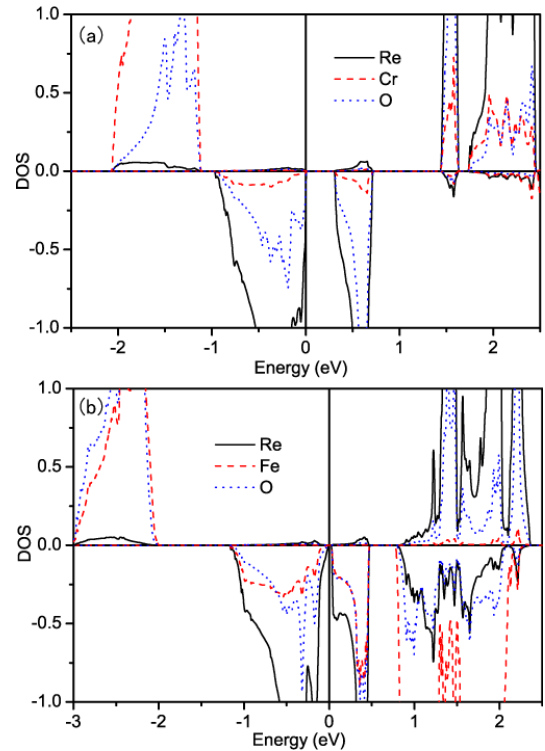


FIG. 9: (color online) The spin-resolved DOSs of $\text{Ca}_2\text{CrReO}_6$ (a) and $\text{Ca}_2\text{FeReO}_6$ (b) calculated with mBJ potential and SOC taken into account.

in the Ca_2MReO_6 calculated with SOC are plotted in Fig. 9. In the presence of SOC, the bands in both of the spin channels hybridize with each other, in contrast to the pictures in Figs. 3 and 4. The Re t_{2g} states around the Fermi level in one spin channel induce some states in the opposite spin channel, especially in the $\text{Ca}_2\text{FeReO}_6$ compound. Moreover, the Re t_{2g} characteristic states with SOC are broadened compared with those without SOC, which leads to the some reduction of the semiconductor gaps of the Ca_2MReO_6 . It should be pointed out that the noninteger moments in Bohr magneton in the Ca_2MReO_6 ($M=\text{Cr,Fe}$) with $P2_1/n$ structure are the consequence of the mixing of spin-up and spin-down states, but the semiconductor gaps are preserved.

VI. CONCLUSION

We have used FP-LAPW method to investigate the structural, electronic, and magnetic properties of double perovskites Ca_2MReO_6 ($M=\text{Cr,Fe}$). The GGA approach has been used to do geometry optimization, and then the electronic and magnetic properties have been investigated with mBJ exchange potential for improving on description of electronic structures. Our calculated results shows that the ground-state phase assumes the $P2_1/n$ structure and is a ferrimagnetic semiconductor for both of the Ca_2MReO_6 , being consistent with ex-

periment. In the case of the $\text{Ca}_2\text{CrReO}_6$ ($\text{Ca}_2\text{FeReO}_6$) phase, we have three (five) Cr^{3+} (Fe^{3+}) 3d electrons and two Re^{5+} 5d electrons, respectively. The Hund's rule and the crystal field and spin exchange splitting require that three Cr^{3+} (Fe^{3+}) 3d t_{2g} ($t_{2g}+e_g$) bands below the Fermi level in the majority-spin channel are fully filled and three Re^{5+} 5d t_{2g} bands astride the Fermi level in the minority-spin channel are filled by two electrons, as the GGA electronic structures shows. Our calculation and comparison shows that the better mBJ exchange potential than GGA and the monoclinic lattice distortion against the $I4/m$ structure are both necessary to obtaining the nonzero semiconductor gaps. This implies that the electron correlations are important in driving the $I4/m$ structure to the monoclinic structure and the resulting cooperation of oxygen-octahedral distortions and electron correlations in the monoclinic phases is necessary to splitting the partially-filled Re 5d triplet bands into the fully-filled doublet bands and the empty singlet bands in the minority-spin channel. In this sense, both electron correlations and O-octahedral distortion are needed for forming the semiconductive nature of the Ca_2MReO_6 . When the spin-orbit coupling is taken into account, the total magnetic moments become noninteger

in unit of Bohr magneton due to the mixing of spin-up and spin-down states, and fortunately, the semiconductor gaps (0.31 and 0.03 eV) remain open.

In summary, our calculated results and analyses show that the monoclinic $\text{Ca}_2\text{CrReO}_6$ and $\text{Ca}_2\text{FeReO}_6$ are both ferrimagnetic semiconductors, being consistent with experiment, and their nonzero semiconductor gaps are formed because there exist strong interaction of oxygen-octahedral distortion and electron correlations in the material. This mechanism can be useful to fully understand chemical and physical properties of double perovskite compounds.

Acknowledgments

This work is supported by Nature Science Foundation of China (Grant No. 11174359), by Chinese Department of Science and Technology (Grant No. 2012CB932302), and by the Strategic Priority Research Program of the Chinese Academy of Sciences (Grant No. XD-B07000000).

* Corresponding author: bgliu@iphy.ac.cn

- ¹ S. A. Wolf, D. D. Awschalom, R. A. Buhrman, J. M. Daughton, S. von Molnár, M. L. Roukes, A. Y. Chtchelkanova, and D. M. Treger, *Science* **294**, 1488 (2001).
- ² M. T. Anderson, K. B. Greenwood, G. A. Taylor, and K. R. Poeppelmeier, *Prog. Solid State Chem.* **22**, 197 (1993).
- ³ K. I. Kobayashi, T. Kimura, H. Sawada, K. Terakura, and Y. Tokura, *Nature (London)* **395**, 677 (1998).
- ⁴ W. E. Pickett, *Phys. Rev. B* **57**, 10613 (1998).
- ⁵ K. I. Kobayashi, T. Kimura, Y. Tomioka, H. Sawada, K. Terakura, and Y. Tokura, *Phys. Rev. B* **59**, 11159 (1999).
- ⁶ A. Arulraj, K. Ramesha, J. Gopalakrishnan, and C. N. R. Rao, *J. Solid State Chem.* **155**, 233 (2000).
- ⁷ Y. Moritomo, S. Xu, A. Machida, T. Akimoto, E. Nishibori, M. Takata, and M. Sakata, *Phys. Rev. B* **61**, R7827 (2000).
- ⁸ M. G. Hernández, J. L. Martinez, and J. A. Alonso, *Phys. Rev. Lett.* **86**, 2443 (2001).
- ⁹ H. Kato, T. Okuda, Y. Okimoto, Y. Tomioka, K. Oikawa, T. Kamiyama, and Y. Tokura, *Phys. Rev. B* **69**, 184412 (2004).
- ¹⁰ G. Vaitheeswaran, V. Kanchana, and A. Delin, *Appl. Phys. Lett.* **86**, 032513 (2005).
- ¹¹ N. S. Rogado, J. Li, A. W. Sleight, and M. A. Subramanian, *Adv. Mater.* **17**, 2225 (2005).
- ¹² A. J. Hauser, R. E. A. Williams, and F. Yang, *Phys. Rev. B* **83**, 014407 (2011).
- ¹³ H. P. Wu, Y. Qian, and R. F. Lu, *Appl. Phys. Lett.* **99**, 123116 (2011).
- ¹⁴ A. Winkler, N. Narayanan, D. Mikhailova, K. G. Bramnik, H. Ehrenberg, H. Fuess, G. Vaitheeswaran, V. Kanchana, F. Wilhelm, A. Rogalev, A. Kolchinskaya, and L. Alff, *New J. Phys.* **11**, 073047 (2009).
- ¹⁵ O. Erten, O. N. Meetei, A. Mukherjee, M. Randeria, N. Trivedi, and P. Woodward, *Phys. Rev. Lett.* **107**, 257201 (2011).
- ¹⁶ A. F. Garcia-Flores, A. F. L. Moreira, U. F. Kaneko, F. M. Ardito, H. Terashita, M. T. D. Orlando, J. Gopalakrishnan, K. Ramesha, and E. Granado, *Phys. Rev. Lett.* **103**, 177202 (2012).
- ¹⁷ C. Du, R. Adur, H. Wang, A. J. Hauser, F. Yang, and P. C. Hammel, *Phys. Rev. Lett.* **110**, 147204 (2013).
- ¹⁸ D. Serrate, J. M. De Teresa, and M. R. Ibarra, *J. Phys.: Condens. Matter* **19**, 023201 (2007).
- ¹⁹ T. K. Mandal, C. Felser, M. Greenblatt, and J. Kübler, *Phys. Rev. B* **78**, 134431 (2008).
- ²⁰ H. Kato, T. Okuda, Y. Okimoto, Y. Tomioka, Y. Takenoyama, A. Ohkubo, M. Kawasaki, and Y. Tokura, *Appl. Phys. Lett.* **81**, 328 (2002).
- ²¹ Y. Kronkenberger, K. Mogare, M. Reehuis, M. Tovar, M. Jansen, G. Vaitheeswaran, V. Kanchana, F. Bultmark, A. Delin, F. Wilhelm, A. Winkler, and L. Alff, *Phys. Rev. B* **75**, 020404(R) (2007).
- ²² O. N. Meetei, O. Erten, M. Randeria, N. Trivedi, and P. Woodward, *Phys. Rev. Lett.* **110**, 087203 (2013).
- ²³ H. L. Feng, M. Arai, Y. Matsushita, Y. Tsujimoto, Y. Guo, C. I. Sathish, X. Wang, Y. H. Yuan, M. Tanaka, and K. Yamaura, *J. Am. Chem. Soc.* **136**, 3326 (2014).
- ²⁴ H. Wang, S. Zhu, X. Ou, and H. W. Phys. Rev. B **90**, 054406 (2014).
- ²⁵ A. K. Pual, M. Jansen, B. Yan, C. Felser, M. Reehuis, and P. M. Abdala, *Inorg. Chem.* **52**, 6713 (2013).
- ²⁶ A. K. Paul, M. Reehuis, V. Ksenofontov, B. Yan, A. Hoser, D. M. Többens, P. M. Abdala, P. Adler, M. Jansen, and C. Felser, *Phys. Rev. Lett.* **111**, 167205 (2013).
- ²⁷ H. Kato, T. Okuda, Y. Okimoto, Y. Tomioka, K. Oikawa

- T. Kamiyama, and Y. Tokura, *Phys. Rev. B* **65**, 144404 (2002).
- ²⁸ F. Tran and P. Blaha, *Phys. Rev. Lett.* **102**, 226401 (2009).
- ²⁹ D. J. Singh, *Phys. Rev. B* **82**, 155145 (2010); **82**, 205102 (2010).
- ³⁰ S. Gong and B. G. Liu, *Phys. Lett. A* **375**, 1477 (2011); *Chin. Phys. B* **21**, 057104 (2012).
- ³¹ S. D. Guo and B. G. Liu, *Chin. Phys. B* **21**, 017101 (2012).
- ³² P. Hohenberg and W. Kohn, *Phys. Rev.* **136**, B864 (1964).
- ³³ W. Kohn and L. J. Sham, *Phys. Rev.* **140**, A1133 (1965).
- ³⁴ P. Blaha, K. Schwarz, G. K. H. Madsen, D. Kvasnicka, and J. Luitz, *WIEN2k an Augmented Plane Wave + Local Orbitals Program for Calculating Crystal Properties* (Karlheinz Schwarz Technische Universität Wien, Austria, 2001).
- ³⁵ J. P. Perdew, K. Burke, and M. Ernzerhof, *Phys. Rev. Lett.* **77** 3865 (1996).
- ³⁶ A. H. MacDonald, W. E. Pickett, and D. D. Koelling, *J. Phys. C: Solid State Phys.* **13**, 2675 (1980).
- ³⁷ J. Kunes, P. Novak, R. Schmid, P. Blaha, and K. Schwarz, *Phys. Rev. B* **64**, 153102 (2001).
- ³⁸ D. D. Koelling and B. N. Harmon, *J. Phys. C: Solid State Phys.* **10** 3107 (1977).
- ³⁹ J. Gopalakrishnan, A. Chattopadhyay, S. B. Ogale, T. Venkatesan, R. L. Greene, A. J. Millis, K. Ramesha, S. Hannoyer, and G. Marest, *Phys. Rev. B* **62**, 9538 (2000).
- ⁴⁰ Z. Szotek, W. M. Temmerman, A. Svane, L. Petit, and H. Winter, *Phys. Rev. B* **68**, 104411 (2003).
- ⁴¹ H. Iwasawa, T. Saitoh, Y. Yamashita, D. Ishii, H. Kato, N. Hamada, Y. Tokura, and D. D. Sarma, *Phys. Rev. B* **71**, 075106 (2005).
- ⁴² D. Koller, F. Tran, and P. Blaha, *Phys. Rev. B* **83**, 195154 (2011).
- ⁴³ J. B. Philipp, P. Majewski, L. Alff, A. Erb, R. Gross, T. Graf, M. S. Brandt, J. Simon, T. Walther, W. Mader, S. Topwal, and D. D. Sarma, *Phys. Rev. B* **68**, 144431 (2003).
- ⁴⁴ J. A. Alonso, M. T. Casais, M. J. Martínez-Lope, J. Martínez, P. Velasco, A. Muñoz, and M. T. Fernández-Díaz, *Chem. Mater.* **12**, 161 (2000).